# RESEARCH PAPERS

*Acta Cryst.* (1998). A**54**, 147–157

## High-Precision Measurement of Temperature Factors for NiAl by Convergent-Beam Electron Diffraction

W. NÜCHTER, A. L. WEICKENMEIER* AND J. MAYER

*Max-Planck-Institut für Metallforschung, Seestrasse 92, D-70174 Stuttgart, Germany.*
*E-mail: weickenmeier@vaxww1.mpi-stuttgart.mpg.de*

(*Received 11 April 1997; accepted 7 August 1997*)

### Abstract

Convergent-beam electron diffraction is applied to measure the temperature factors of the intermetallic phase NiAl with high accuracy. The patterns are recorded in an energy-filtering transmission electron microscope at zero energy loss using a slow-scan CCD camera. The specimens were tilted in systematic row orientation. In this new approach, data are extracted from the bright-field disc as well as from several high-order dark-field discs along line scans. The temperature factors are determined by fitting Bloch-wave simulations to the intensity profiles. The harmonic approximation for temperature factors is used. For *B*2-phase NiAl, mean thermal displacements $u(\mathrm{Ni}) = 5.5 \pm 0.1$ and $u(\mathrm{Al}) = 5.7 \pm 0.1$ pm are obtained at 100 K. A very detailed error analysis is given, and stochastic and systematic errors are discussed and quantified.

### 1. Introduction

Convergent-beam electron diffraction (CBED) nowadays is appreciated as a very valuable tool for quantitatively determining crystal data such as lattice constants, atomic positions and structure factors. Here we report a new application, the high-precision determination of temperature factors (TFs).

Temperature factors, also referred to as Debye–Waller factors, play a central role in the simulation of diffraction patterns and high-resolution images. They incorporate the influence of the thermal motion of the atoms by a smearing out of the real potential and as an absorption potential. Comparison with experimental high-precision TF data also provides a comprehensive test for molecular dynamics simulations (Gumbsch & Finnis, 1996).

The most challenging enterprise in CBED is the accurate measurement of structure factors from which the bond charge density can be derived. However, for the conversion of the measured crystal potentials to electron densities, a very precise knowledge of the TFs is indispensable.

TFs are usually found in X-ray literature since they are determined along with the crystal structure data on a routine basis. For NiAl, TFs have been measured by Cooper (1963), Hughes, Lautenschlager, Cohen & Brittain (1971), Georgopoulos & Cohen (1977) and Menon & Fox (1996). Unfortunately, these data were determined at room temperature, whereas quantitative CBED is preferably performed at liquid-nitrogen temperature. This helps to keep thermal diffuse scattering at a minimum level and also to reduce specimen contamination.

Inspecting the data, we observed that the results show a remarkable spread of about 20%. This is probably due to the limited accuracy of powder experiments (Cooper, 1963) or the use of low-order reflections in single-crystal measurements (Hughes, Lautenschlager, Cohen & Brittain, 1971). Very precise powder data have been obtained by Menon & Fox (1996) using an improved extinction-correction scheme. Their results are in close agreement with the single-crystal measurements of Georgopoulos & Cohen (1977). These workers employed more than 100 high-order reflections and therefore obtained highly reliable results. However, single-crystal experiments require relatively large specimens and are thus prone to errors due to crystal imperfections. It is the intrinsic advantage of CBED that probe diameters of less than 20 nm are easily realized by working with a focused beam, and the specimen area under observation can be checked for imperfections by switching to the imaging mode.

From the quantitative evaluation of CBED patterns of perfect crystals, very detailed information such as atomic positions, charge density, temperature factors and lattice constants can be derived (Spence & Zuo, 1992). Techniques to measure structure factors have been reported by Bird & Saunders (1992) for zone-axis orientation and Zuo & Spence (1991) in systematic row orientation. Recently, Holmestad, Zuo, Spence, Hoier & Horita (1995) studied the influence of Mn doping on the charge density of TiAl. Swaminathan, Jones, Maher, Johnson & Fraser (1997) analysed the effects of TFs and composition on the 200 structure factor in TiAl.

For NiAl, first TF measurements with CBED have been performed by Fox (1983) using the critical-voltage

(CV) technique. This method is extremely sensitive to the absolute value of low-order structure factors. Therefore, provided the zero-temperature structure factors are known, the TFs can be derived with high accuracy. Unfortunately, only the low-order structure factors can be investigated. Thus, the influence of bonding effects cannot properly be disentangled from the TF effects. In a more advanced approach, Matsumara, Tomokiyo & Oki (1989) combined the CV with the intersecting Kikuchi-line (IKL) technique for f.c.c. metals. In favourable cases, the errors can significantly be reduced. The problem of the bonding influence, however, cannot be overcome.

More recent experiments are based on the application of energy filters, which makes it possible to remove most of the inelastically scattered electrons. Therefore, patterns are solely recorded with electrons that have undergone elastic or thermal diffuse scattering. Only these patterns can be simulated with high accuracy, allowing the extraction of quantitative data.

Burgess *et al.* (1994) used the zone-axis technique (Bird & Saunders, 1992) to fit a set of low-order structure factors of Ge, including 400 and 113 (which they assumed to be very close to the free-atom values) using various TFs. They concluded that from the fit which reproduces the free-atom values they can deduce the correct TF. The sensitivity, however, seems to be low.

Lehmpfuhl, Krahl & Uchida (1995) simulated the intensity distribution of large-angle CBED patterns for three different zone axes of Si. They compared the dynamical shift of various high-order lines with experiments to deduce the TFs. This technique works with a simple by-eye comparison of simulation and experiment, which is a major advantage compared with techniques which require extensive computing.

In a different approach, Holmestad, Weickenmeier, Zuo & Horita (1993) tried to determine TFs of TiAl from the intensity distribution in CBED patterns. Intensities of high-order reflections at exact Bragg position were extracted and the TFs determined by means of the Wilson plot. As discussed in their paper, the purely kinematical approach turned out to be not accurate enough. This has also been observed and addressed by Preston, Burgess, Pickup & Humphreys (1993) who derived TFs for silicon at room temperature from unfiltered and filtered large-angle convergent-beam (LACBED) patterns with the same technique.

In the next step, Holmestad, Weickenmeier, Zuo & Horita (1993) used the Bethe potential corrections. They obtained a significant improvement of the Wilson-plot results. This technique, however only works in near-two-beam-like beam orientations and for thin specimens. It also only yields an average TF, since different atomic species as well as non-equivalent crystallographic sites cannot be accounted for.

The most elaborate approach is to extract complete rocking curves of various high-order reflections from one pattern. These line scans typically consist of 1000 data points. For TiAl, TFs have been determined by Holmestad, Weickenmeier, Zuo, Spence & Horita (1993) by manually adjusting simulations to the experimental data. Zuo, Holmestad, Tomokiyo & Yase (1995) have measured a set of low- and medium-order structure factors of MgO. They plotted the logarithmic ratio of the measured and zero-temperature free-atom structure factors as a function of the squared reciprocal-lattice vector. From the slope of this plot, they derived an average TF. They found it impossible to derive individual TFs for Mg and O because of bonding effects on the reference structure factors.

In our approach, we have implemented a fully automated fitting procedure which allows the determination of the TFs, specimen thickness and incident-beam direction on an absolute scale with high precision from high-order reflections. Here we report our experiments on the intermetallic phase NiAl. We primarily focus on the technique but will also discuss error sources and principal limitations.

## 2. Temperature factors

The intensity distribution in electron diffraction patterns depends on temperature through the structure factors (Fourier coefficients of the crystal potential) as well as through thermal diffuse scattering, which causes a weakening of the Bragg reflections.

In general, the structure factors are given by (Willis & Pryor, 1975)

$$U_{\mathbf{g}} = (1/\Omega) \sum_j f_j(\mathbf{g}) T_j(\mathbf{g}) \exp[i\mathbf{g}\mathbf{R}_j]. \qquad (1)$$

Here, $\Omega, f_j, T_j$ and $\mathbf{R}_j$ denote the volume of the unit cell, the Fourier transform of the atomic potential, the TF and the position vector of atom $j$, respectively.

For temperature well below the Debye temperature, the harmonic approximation holds. Then we may write

$$T_j(\mathbf{g}) = \exp[-\tfrac{1}{2}\langle(\mathbf{g}\mathbf{u}_j)^2\rangle], \qquad (2)$$

$\mathbf{u}_j$ being the instantaneous thermal displacement of atom $j$ and $\langle\ \rangle$ denoting the average. Depending on the site symmetry, (2) can be simplified, *e.g.* in the case of NiAl we have cubic site symmetry for both atomic species and (2) reduces to

$$T_j(\mathbf{g}) = \exp[-\tfrac{1}{2}\langle u_j^2\rangle g^2]. \qquad (3)$$

Therefore, it is sufficient to determine one parameter per atom, the mean square thermal displacement $\langle u_j^2\rangle$.

The Fourier coefficients of the atomic potential in (1) are approximated by those calculated for spherical neutral atoms (Rez, Rez & Grant, 1994). This is only an approximation since bonding effects are completely ignored. However, for high-angle reflections, the influence of bonding on the structure factors is small compared with the temperature dependence.

It has been shown by Yoshioka (1957) that in a first-order approximation an absorption potential can account for the removal of electrons from the Bragg reflections by inelastic scattering processes. For thermal diffuse scattering, the corresponding absorption potential has been derived by Hall & Hirsch (1965). Employing the Einstein approximation, they obtained

$$U'_{\mathbf{g}} = -(1/kV)\sum_j \exp[i\mathbf{g}\mathbf{R}_j]\int \mathrm{d}^2\mathbf{q}\, f_j(\mathbf{q}) f_j(\mathbf{q}-\mathbf{g}) \times \{\exp[-\tfrac{1}{2}\langle u_j^2\rangle g^2] - \exp[-\tfrac{1}{2}\langle u_j^2\rangle \mathbf{q}^2] \times \exp[-\tfrac{1}{2}\langle u_j^2\rangle(\mathbf{q}-\mathbf{g})^2]\}, \quad (4)$$

which also only depends on the mean squared thermal displacements $\langle u_j^2\rangle$.

## 3. Computation of CBED patterns

For the simulation of CBED patterns, the Schrödinger equation is most efficiently solved in Fourier space. The wave function of the fast electron is then given by

$$\Psi(\mathbf{r}) = \sum_{j\mathbf{g}} \varepsilon^{(j)} c_{\mathbf{g}}^{(j)} \exp[i(\mathbf{k}^{(j)} + \mathbf{g})\mathbf{r}]. \quad (5)$$

The excitation coefficients $\varepsilon^{(j)}$ are chosen to satisfy the boundary conditions, the wave vectors $\mathbf{k}^{(j)}$ and coefficients $c_{\mathbf{g}}^{(j)}$ are found by solving the dispersion equation of the dynamical theory

$$[(\mathbf{k}^{(j)} + \mathbf{g})^2 - k^2] c_{\mathbf{g}}^{(j)} = \sum_{\mathbf{h}} \mathcal{U}_{\mathbf{gh}} c_{\mathbf{h}}^{(j)} \quad (6)$$

for each beam direction. The potential matrix $\mathcal{U}_{\mathbf{gh}}$ is set up from the structure factors and the absorption

$$\mathcal{U}_{\mathbf{gh}} = U_{\mathbf{g}-\mathbf{h}} + iU'_{\mathbf{g}-\mathbf{h}} \quad (7)$$

and thus contains the temperature dependence of the CBED pattern. Since many computer codes already exist for the solution of (6), we only summarize briefly the most important details of our calculations.

Only a limited number of reflections $\mathbf{g}$ can be included in the calculations. To ensure the most efficient computation, we follow the automated beam-selection scheme suggested by Zuo & Weickenmeier (1995). Only those reflections with structure factor larger than a given minimum are considered. Depending on excitation error and structure factor, beams are selected for diagonalization or treated as perturbation by means of the Bethe correction. A very detailed discussion of how convergence of the computation is achieved and controlled was given by Zuo & Weickenmeier (1995).

A complete set of Fourier transformed atomic potentials for neutral atoms $f_j(\mathbf{q})$ has been computed by Rez, Rez & Grant (1994) using a self-consistent Dirac–Fock–Slater code. These data are very close to the most commonly used Doyle & Turner (1968) tables, which represent the output of various programs.

For the absorptive part of the potential, only phonon scattering is considered. Actual values of $U'_{\mathbf{g}-\mathbf{h}}$ are computed with the *FSCATT* program (Weickenmeier & Kohl, 1991), which is based on the analytical solution of (4).

The solution of (6) involves the determination of eigenvalues and eigenvectors of a complex general matrix. This is done with a double-precision routine taken from the *EISPACK* package to achieve numerical stability.

## 4. Experiment

The material we investigated is the ordered intermetallic phase NiAl-*B*2, which is of technical interest as a high-performance material at elevated temperatures. The structure of NiAl is CsCl type, the space group is *Pm*3*m* (No. 227). The lattice constant of 2.882 Å at 110 K was calculated using the thermal-expansion coefficient measured by Sandakova, Sandakov, Kalishevich & Gel'd (1971). Since this value allowed the positions of higher-order Laue-zone (HOLZ) lines to be fitted with sufficient accuracy, no attempt has been made to measure the lattice constant independently by CBED techniques.

The NiAl single crystals were produced in the Max-Planck-Institut für Metallforschung by Essmann, Henes, Holzwarth, Klopfer & Büchler (1997). Ingots were produced from Al and Ni of 99.998% purity. To compensate for non-stoichiometric evaporation of Al, a surplus of 0.1% Al was added to the nominal composition. The melting and mixing is performed in an alumina crucible by induction heating in a high-purity argon atmosphere. The melt is then cast into copper moulds of 60 mm length and 20 mm diameter. Then, the ingots are cleaned in a mixture of 100 ml acetic acid, 60 ml nitric acid, 20 ml sulfuric acid and 20 ml phosphoric acid at about 363 K. Finally, they were annealed for 6 h at 923 K, 2.5 h at 1023 K, and 42 h at 773 K. Chemical composition (stoichiometry) was checked by wet chemical analysis and found to be 50:50.

From the NiAl rods, slices of thickness 5 mm were cut by spark erosion. After mechanical thinning to 100 μm, specimens of 3 mm diameter were punched out and electropolished in a 50:1 mixture of ethanol and perchloric acid at 243 K until electron transparency was reached.

The CBED patterns were recorded in the energy-filtering Zeiss EM912 Omega transmission electron microscope at an acceleration voltage of 120 kV. Patterns were filtered at zero energy loss with an energy window of 5–10 eV. In order to reduce contamination and thermal diffuse scattering, the specimens were cooled down to liquid-nitrogen temperature. The patterns were acquired with a Gatan model 679 slow-scan CCD camera equipped with an anti-reflection YAG scintillator providing 1024 × 1024 pixels. The modulation transfer

function (MTF) of the camera has been measured (Weickenmeier, Nüchter & Mayer, 1995) and was deconvoluted from the patterns.

Preliminary experiments showed that maximum sensitivity to temperature factors is obtained if both the intensity in the bright-field disc as well as in at least three high-order dark-field discs is recorded. In the experiments, we tilted the specimen in a systematic row orientation and used a convergence angle of about twice to three times the Bragg angle, in which case the pattern shows three to four adjacent **g** discs with each reflection **g** in Bragg position. To provide sufficient resolution (since the number of pixels is limited), we always take two frames, one for the bright-field and one for the dark-field discs, respectively, using the post-specimen deflection coils to shift the diffraction pattern across the camera.

## 5. Data refinement

The intensity distribution in a CBED pattern is determined by incident-beam direction, specimen thickness and the interaction potential of the fast electron with the crystal. Once all these parameters are known, the computation of the pattern is straightforward. In the evaluation of experimental patterns, we face the reverse problem: the experimental pattern is known and the parameters are to be found.

In the refinement procedure, the CBED patterns are computed based on a given set of parameters. The patterns are then compared pixel by pixel with experimental data, employing an objective measure of the difference (*e.g.* a $\chi^2$ test). On an iterative basis, the input parameters are varied in order to obtain the best match between simulation and experiment. The parameters of interest as well as an error estimate are taken from the best match. In this section, we want to explain the details of the matching process.

### 5.1. *Fit parameters*

The parameters required to compute a CBED pattern can be divided into two groups: (i) the geometrical parameters including the high voltage (defining the beam orientation and magnification of the patterns) and (ii) the specimen parameters (thickness and TFs).

To be able to compare the experiment and simulation, we have to associate each pixel in each disc of the experimental pattern with a beam direction. To do so, we determine the coordinates of a reference point and the two components of a **g** vector. Also, if we take the bright-field disc and the dark-field discs in two subsequent frames, we have to determine the shift vector. Therefore, we need to find six geometrical parameters.

Before putting these parameters into the pattern-matching algorithm, we usually perform a pre-determination. Firstly, a quick and sometimes rather rough estimate for the reference point can be obtained on the basis of pure kinematical calculations, which subsequently can be refined by simple eye inspection using a full dynamical simulation. An estimate of a reciprocal-lattice vector **g** is readily found by simply measuring the distance between the centres of the diffraction discs in the experimental pattern.

The interaction of the specimen with the fast electron is governed by the potential matrix $\mathcal{U}_{\mathbf{gh}}$, which (since atomic positions and atomic potential are fixed) only depends on the TFs of Ni and Al, respectively. Thus, we have to refine two more parameters. Therefore, in total, eight parameters are to be found.

Moreover, the intensity distribution also depends on the specimen thickness. However, once the electron wave function has been determined (*i.e.* the eigenvalue problem has been solved), it only costs a little extra time to compute the intensity for a set of, say, a hundred thicknesses in steps of 5 Å. Therefore, the thickness that yields the best match can readily be found without treating it as a fit parameter.

The high voltage is determined from an independent measurement. Before and after taking the CBED patterns of NiAl, we insert a standard Si specimen. CBED patterns are taken in the (331) zone-axis orientation. By comparison with a series of dynamical simulations for various high voltages, the high voltage can readily be determined with the required accuracy of 100 V.

### 5.2. $\chi^2$ *test*

At each stage of the iterative parameter adjustment, the simulated and experimental patterns need to be compared. In order to quantify the difference objectively, a mathematical measure is employed. The measure preferred by most groups working on quantitative CBED is the $\chi^2$ test, since the Poisson noise of the electrons as well as the detector noise are inherently considered. $\chi^2$ is most commonly defined as

$$\chi^2 = [1/(N-f-1)] \sum_{i=1}^{N} [(I_i^{\mathrm{exp}} - cI_i^{\mathrm{theo}})^2/\sigma_i^2]; \quad (8)$$

however, to also take account of the background, we use a slight modification:

$$\chi^2 = [1/(N-f-1)] \sum_{i=1}^{N} [(I_i^{\mathrm{exp}} - cI_i^{\mathrm{theo}} - B_i)^2/\sigma_i^2]. \quad (9)$$

Here, $N$ and $f$ denote the number of pixels to be compared and the number of parameters that are adjusted, respectively. $I_i^{\mathrm{exp}}$ is the experimental, $I_i^{\mathrm{theo}}$ the simulated intensity and $\sigma_i$ the noise in pixel $i$. Since the simulated intensity is normalized to unity, we need a scaling constant $c$. The background in each pixel is denoted by $B_i$. The latter parameters are not part of the fit procedure but determined as follows: for each set of simulated intensities $I_i^{\mathrm{theo}}$, the values of $c$ and $B_i$ (positive numbers) that

minimize $\chi^2$ are calculated exploiting analytical formulas. Hereby, the background level $B_i$ is constant within each disc, but for different discs different levels are allowed. Alternatively, the background values can also be estimated from the CBED pattern and kept fixed during the refinement.

The noise in each pixel $\sigma_i$ is due to the Poisson statistics of the incoming electrons combined with the noise amplification of the detection system (*i.e.* the CCD camera). We analysed a set of noise images, acquired with uniform illumination and different exposure times (Weickenmeier, Nüchter & Mayer, 1995). We found that after deconvolution the noise as a function of the intensity can be approximated by

$$\sigma^2 = (1.6 + 2.26 \times 10^{-5} \times I^{\exp})I^{\exp}. \quad (10)$$

In order to shed some more light on the $\chi^2$ test, we assume that the experimental signal is given by

$$I_i^{\exp} = cI_i^{\text{theo}} + B_i + \sigma_i + \Delta_i, \quad (11)$$

where $\sigma$ is the noise and $\Delta$ a systematic error. Then, for the typical case of $N \gg f$, we have to a very good approximation

$$\chi^2 = 1 + (1/N)\sum_{i=1}^{N} \Delta_i^2/\sigma_i^2. \quad (12)$$

Thus, a $\chi^2$ value of 1 means a perfect match and the $\chi^2$ test is normalized. In the presence of systematic errors, however, the $\chi^2$ value depends on the count rate, since the fraction $\Delta^2/\sigma^2$ scales linearly with the intensity. It is difficult to judge the goodness of fit from the numerical $\chi^2$ value and to compare the reliability of various experiments.

There is one more drawback with the $\chi^2$ test. We may understand the factor $1/\sigma_i^2$ as a weighting factor. Since low-intensity pixels show the largest errors due to dark-current subtraction (CCD camera) and thermal diffuse background, there is too much weight on these pixels, compared with the high-intensity pixels. However, when switching from (8) to (9), the relative influence of low-intensity pixels is reduced.

The $\chi^2$ test also provides a possibility for an error estimation. From a formal point of view, $\chi^2$ depends on a set of parameters $a_i$ (*i.e.* beam-orientation parameters, TFs). Then, the error in $a_i$ can be estimated as (Wolberg, 1967)

$$\delta a_i = (\chi^2)^{1/2}(C_{ii})^{1/2}, \quad (13)$$

where $C$ is the inverse of the $\alpha$ matrix given by

$$\alpha_{kl} = \tfrac{1}{2}\partial^2\chi^2/\partial a_k \partial a_l. \quad (14)$$

We want to stress the point that this error estimate is solely based on the statistical nature of the signal. It does not account for any systematic errors and thus will tend to underestimate the real error.

### 5.3. *Minimization strategies*

The determination of a set of physical parameters from a given experiment is reformulated as a multidimensional nonlinear minimization problem: find the parameter set that minimizes the $\chi^2$ function. As usual in nonlinear multiparameter fitting problems, more than one minimum exists. This has been observed in previous studies (Deininger, Necker & Mayer, 1994) as well as in our present investigations. The physical parameters we are interested in are those that correspond to the absolute minimum. To deal with this problem, two aspects have to be considered. Firstly, the actual shape of the $\chi^2$ landscape will depend on the intensities $I_i^{\exp}$ we extract from the experimental pattern. Secondly, it is worthwhile applying some care when selecting from the variety of minimization algorithms.

A CBED pattern captured with a CCD camera consists of $1024 \times 1024$ pixels and typically shows three different discs with a diameter of roughly 300 pixels. Thus we have about 200 000 data points to choose from in the dark-field discs and bright-field disc. Unfortunately, even with modern high-speed computers, we have to limit the number of pixels put into the $\chi^2$ test to about 1000. The common strategy therefore is to extract a simple line scan across the discs in a systematic row. It turned out that, in particular for thick specimens, this choice of data points generates multiple minima in the $\chi^2$ function (Deininger, Necker & Mayer, 1994). From our experience, the following strategy is favourable in order to generate a smooth $\chi^2$ landscape. We use a specimen thickness so that the rocking-curve fringes are resolved by the camera (while displaying about three discs), which facilitates the thickness determination. We try to fix the beam direction by using at least two scans along the maximum intensity (along the Bragg position) and another two across the discs to prevent the algorithm from rotating and shifting the pattern. Thus, less local minima exist, in which wrong values of the TFs are partially compensated by a wrong beam direction and specimen thickness. An example for our line-scan placement strategy can be found in the next section.

The presence of several minima makes it tempting to tackle the problem with a global optimizer, such as simulated annealing (Ingber, 1989) or related algorithms. However, after extensive testing, we found that, on the one hand, these strategies are extremely inefficient in the vicinity of minima and, on the other hand, they do not locate the absolute minimum with sufficient reliability in acceptable computing time. Thus, we prefer a non-gradient-based one-dimensional minimizer, which is applied to each parameter in turn. The cycle is repeated until the decrease in $\chi^2$ is smaller than a tolerance. It typically takes 5–10 cycles to achieve convergence. While this technique might not be the most efficient one, it combines acceptable efficiency with general stability. The multiple-minimum problem is solved by restarting the

program several times, each time starting from different values randomly chosen from a given search interval.

## 6. Results

A schematic drawing of a typical experiment is given on the left side of Fig. 1. Typically, three diffraction discs (here four discs 500–800) can be projected on the CCD camera. From those discs, line scans are extracted. As explained in §5.3, the choice of the line-scan placement has an influence on the efficiency of the refinement process. In order to illustrate our strategy of placing line scans, they are marked in Fig. 1 in the recorded patterns. The corresponding intensity data are plotted in Fig. 2, along with the best fit.

With scans *S*1, *S*2, *S*4, *S*5, *S*6, the incident-beam direction along the systematic row and the camera length are fixed, while with *S*3 the beam direction with respect to the direction perpendicular to the systematic row is adjusted. Scans *S*2 and *S*4 prevent the algorithm from rotating the pattern. The relative displacement between the bright-field and the dark-field pattern is determined using *S*7. The geometrical parameters can be found very quickly and without local minima using this strategy. Of course, scans *S*1–*S*6 monitor the intensity of the reflections (*S*1 of the direct beam) and are used to adjust the temperature factors. Another example of our line-scan placement strategy can be found in Nüchter, Weickenmeier & Mayer (1995).

At the bottom of Fig. 2, the contribution $(I_i^{\exp} - cI_i^{\text{theo}} - B_i)/\sigma_i$ of the individual pixel $i$ to $\chi^2$ is plotted. In favourable cases where a good fit has been obtained, this curve does not show systematic variations but only a random fluctuation. Moreover, it becomes clear why the $\chi^2$ function is an excellent choice as an objective measure of the difference between experiment and simulation. On the one hand, we notice that according to the larger absolute value of $\sigma$ for high-intensity signals larger absolute deviations of ($I^{\text{theo}}$ from ($I^{\exp}$ are permitted. On the other hand, since we subtract a background signal, the $\chi^2$ test obviously is not too sensitive to low-signal pixels.

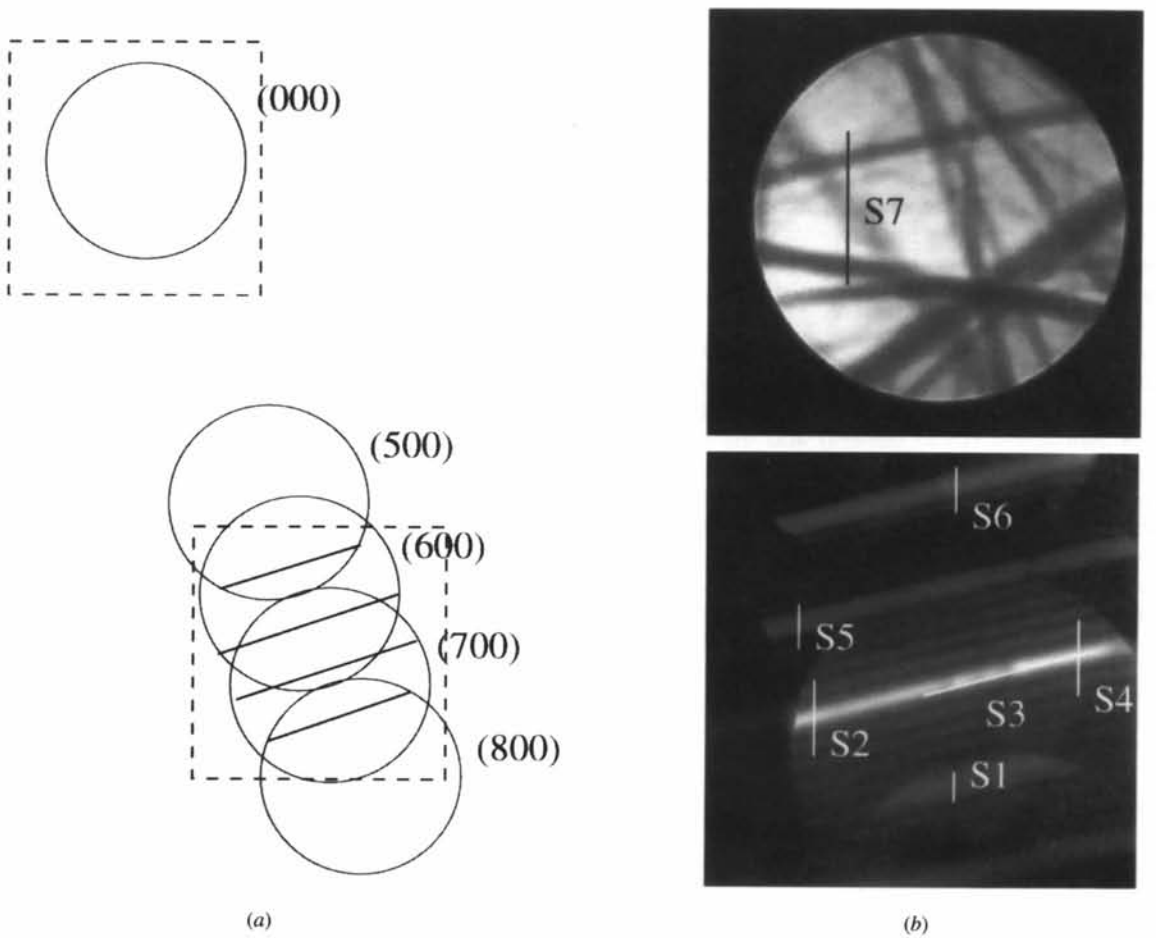


(*a*) (*b*)

Fig. 1. (*a*) A schematic drawing of a typical experiment. The dashed squares show the area covered by the CCD camera. (*b*) The recorded patterns. Inside these patterns, the positions of the line scans are indicated. The corresponding intensities are given in Fig. 2, along with the best fit.

Various measurements have been performed using different specimen areas as well as different specimens in order to avoid specimen-dependent systematic errors (such as deviation from stoichiometry). However, all specimens are prepared with a (110) surface normal to facilitate tilting the same specimen in the (100) and (110) systematic row orientation, respectively. The results of the seven evaluations that led to a $\chi^2$ value lower than 5 are given in Table 1, five other experiments were discarded owing to larger $\chi^2$ values. For each individual experiment, the statistical error as defined in (13) is given in brackets. In the last but one row, the average values and the estimated errors are given. The final results are $u(\mathrm{Ni}) = 5.5 \pm 0.1$ and $u(\mathrm{Al}) = 5.7 \pm 0.1$ pm at $T = 110$ K. The estimated errors are computed as $\sigma/N^{1/2}$. Here $N = 7$ and $\sigma$ is the standard variation of the seven results, defined as the square root of the variance

$$\sigma^2 = [1/(N-1)] \sum_{i=1}^{N} (x_i - \langle x \rangle)^2.$$

The variance is given in the last row. The variance can be used as a measure for the combined systematic and stochastic error for a single experiment. As expected, the standard variation exceeds the statistical errors of most of the individual experiments, owing to systematic errors. These will be discussed in detail in the next section.

## 7. Error discussion

In Table 1, two different errors are given. The first one (in brackets after the individual results) is evaluated using (13) and is based only on the stochastic nature of electron emission. If we were to repeat the experiment under identical conditions $N$ times, then in the limit of $N \to \infty$ the average values of the two different measured temperature factors would converge to the true values for that particular experimental set-up (which may still be influenced by all systematic errors there might be) and the standard deviation would be close to the uncertainty we predicted on the grounds of the well known Poisson statistics.

Repeating the experiment under identical conditions would mean for example taking a series of patterns without changing anything. So for all patterns systematic errors are identical. To estimate the error bars for the temperature factors including the systematic errors, we would have to locate all possible error sources, estimate

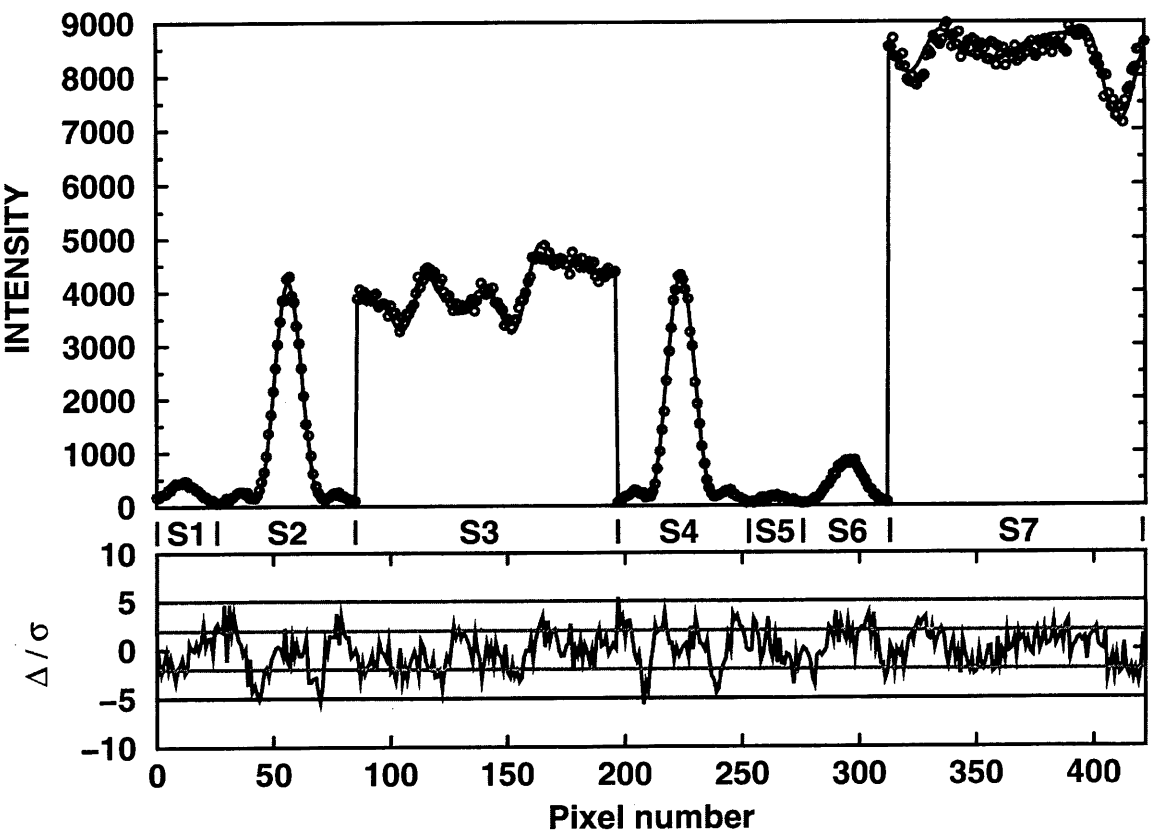


Fig. 2. The intensities of the line profiles shown in Fig. 1, along with the best fit. The $\chi$ value is 3.6. In the lower part, the difference $\Delta$ between experiment and theory is given, scaled by the noise level $\sigma$. Deviations of $|\Delta/\sigma|$ larger than 2–5 would indicated systematic errors of the fitting parameters.

Table 1. *Results for the thermal displacements u at T = 110 K*

In each row, the error based on the stochastic nature of electron emission is given in brackets. In the last but one row, we give the average value and the estimated error of the average; in the last row, the standard deviation of the set. For experiment no. 6, the (000) disc could not be evaluated due to a problem with the data acquisition.

| No. | $\chi^2$ | $u$(Ni) (pm) | $u$(Al) (pm) | Reflections considered | Thickess (nm) |
|---|---|---|---|---|---|
| 1 | 3.9 | 5.0 (2) | 5.5 (5) | (440)–(770), (000) | 47.8 |
| 2 | 3.7 | 5.2 (1) | 5.5 (1) | (500)–(700), (000) | 111.6 |
| 3 | 3.3 | 5.3 (1) | 5.7 (2) | (440)–(660), (000) | 50.1 |
| 4 | 3.5 | 5.5 (1) | 5.4 (2) | (440)–(660), (000) | 68.8 |
| 5 | 2.1 | 5.6 (1) | 5.7 (1) | (440)–(660), (000) | 44.2 |
| 6 | 4.1 | 5.8 (1) | 5.5 (1) | (500)–(800) | 167.9 |
| 7 | 3.6 | 6.0 (1) | 6.2 (1) | (500)–(800), (000) | 43.9 |
| | | 5.5 ± 0.1 | 5.7 ± 0.1 | Average and estimated error | |
| | | 0.4 | 0.3 | Standard deviation | |

their magnitudes and then try to calculate the influence on the temperature factors (for a more detailed discussion see *e.g.* Chapter 4.9 in Wolberg, 1967). However, since we can perform many experiments with different settings of the microscope, using different samples, zone axes and specimen thicknesses, we also sample the statistical distribution of all the systematic errors, which are likely to vary for different measurements. Therefore, for an infinite number of experiments, the influence of the systematic errors is minimized and the average result will be as close to the true result as possible. The remaining differences between the observed average results and the true values are due to systematic errors that cannot be averaged out by that particular kind of experiment (here CBED). The magnitude of these errors still has to be estimated.

In terms of a statistical analysis, the uncertainty in the observed average result decreases as $\sigma/N^{1/2}$, where $\sigma$ is the standard deviation. But the observed result might still be different from the true result. In the following sections, we characterize the most important error sources and try to estimate, if possible, their order of magnitude.

### 7.1. *Specimen temperature*

The specimen is cooled with liquid nitrogen down to a temperature of about 110 K. However, the illuminated area is heated up as a consequence of the inelastic interactions of the fast electrons with the specimen. A rather simple formula, allowing estimation of the rise in temperature, can for example be found in Reimer (1984):

$$\Delta T = (j\rho/2e\lambda)(\Delta Q/\Delta x)r_0^2 \ln(R/r_0). \qquad (15)$$

Here, $j$, $\rho$, $e$, $\lambda$, $r_0$ and $R$ denote the beam current density, specimen density, elementary charge, heat conductivity, spot and specimen radius, respectively. The deposited energy per unit mass thickness, $\Delta Q/\Delta x$, can be estimated using the nonrelativistic Bethe energy-loss formula (see *e.g.* Reimer, 1984)

$$\Delta Q/\Delta x = 7.8 \times 10^4 (Z/A)(1/E)\ln(E/IZ). \qquad (16)$$

If we insert the atom number $Z$ and mass $A$ in units of $(1/12)m(^{12}\mathrm{C})$, the electron energy $E$ and the mean ionization energy $IZ = 13.5Z$ in eV, then we get $\Delta Q/\Delta x$ in units eV cm$^2$ μg$^{-1}$. For our experiment, we have $\lambda$(NiAl) = 80 J (s m K)$^{-1}$, $r_0$ = 10 nm and $R$ = 3 mm. For the biatomic crystal NiAl, we replace the term

$$\rho(\Delta Q/\Delta x) \Rightarrow [\rho(\Delta Q/\Delta x)]_{\mathrm{Ni}} + [\rho(\Delta Q/\Delta x)]_{\mathrm{Al}}.$$

Inserting the electron energy of 120 keV and the beam current density of 6 Å cm$^{-2}$, we obtain $\Delta T$ = 0.0006 K. Therefore, the beam heating effect is certainly negligible.

On the other hand, there are uncertainties in the temperature measurement. The specimen temperature is measured as the temperature difference between the tip of the specimen holder (which according to the manufacturer's manual might be about 2 K lower than the real specimen temperature) and the microscope room. From this difference, a fixed value, the assumed laboratory temperature, is subtracted. Therefore, if the assumed room temperature differs from the real one (this deviation might be of order ±5 K), we have a systematic error of about ±7 K in all of our experiments. Moreover, the room temperature, although controlled by the air-conditioning system, varies within about ±1 K. Also, the temperature the specimen reaches varies in the range 108 to 114 K, depending mainly on the specimen-holder evacuation.

So, in summary, we have a systematic deviation of about $\Delta T = \pm 7$ K plus a random scatter of about $\delta T = \pm 5$ K. The scatter in temperature can be converted to a scatter in the temperature factors employing the calculations of Gumbsch & Finnis (1996), who give the $u_i$ as a function of temperature. Assuming an average temperature of 110 K, a variation of 5 K leads to a $\Delta u$ of 0.05 pm for both Ni and Al.

According to the discussion preceding this paragraph, the average rise of $\Delta T$ is a systematic error, which will be present in all experiments. It cannot be measured but has to be estimated. On the other hand, the variation $\delta T$ of the temperature may be treated as a statistical variable.

### 7.2. *Stoichiometry*

The result of the wet-chemical analysis is that our specimen is stoichiometric 50–50 NiAl. The uncertainty associated with that kind of analysis is about 0.3%. In the case of Ni-rich NiAl, we get Ni antisite atoms, in the other case we have Ni vacancies. The structure factors we use for the simulation are based on a site occupancy of 1 for each site. In the case of 49.7–50.3 NiAl, the true Ni-site occupancy would be $49.7/50.3 = 0.99$. Since the true structure factor is smaller than the supposed one, the refinement program will adjust the temperature factors to compensate for the difference, causing inaccurate results.

A worst case estimate of the influence of this effect can be found as follows: For the situation described above, the true structure factors are given by

$$U_{\mathbf{g}} = (1/\Omega)\{\alpha f_{\mathrm{Ni}} \exp[-\tfrac{1}{2}\langle u^2\rangle_{\mathrm{Ni}} g^2] \pm f_{\mathrm{Al}} \exp[-\tfrac{1}{2}\langle u^2\rangle_{\mathrm{Al}} g^2]\} \quad (17)$$

with $\alpha = 0.99$. The simulation will suppose $\alpha = 1$. In the worst case, this will be compensated by only modifying the Ni temperature factor, resulting in $\Delta u_{\mathrm{Ni}} = 0.1$ pm in the case of the (500) structure factor. This is of the order of the observed standard deviation. However, at least three reflections are used in each refinement process, therefore it is not possible to totally compensate for a change in stoichiometry. The simulation will end up with a higher $\chi^2$ value and a smaller deviation from the true temperature factor than estimated here. Also, (500) is the lowest indexed reflection used for the fits. And, furthermore, both temperature factors will be affected, leading to a smaller deviation for each one. This method for the error estimation seems very rough, however, the order of magnitude of the error becomes clear.

### 7.3. *Surface oxidation*

The final step in the specimen-preparation process is the electropolishing. Once the specimen is taken out of the polishing liquid, the oxidation starts, resulting in an amorphous oxide layer on the specimen surface. The layer thickness has been measured employing the energy-loss spectrum of the specimen, using a technique developed by Mayer, Eigenthaler, Plitzko & Dettenwanger (1997). The first sample was examined immediately after the preparation process and no oxide was detected. For a different sample, which was stored for about 6 months at room conditions, the total oxide layer was about 4 nm thickness including both top and bottom surfaces.

In a first approximation, an amorphous layer will slightly modify the illumination. It is known that for parallel illumination the diffraction pattern of an amorphous specimen consists of a ring system due to the remaining short-range order. So, in a simple picture, each beam in the incoming convergent beam is modified into a slightly weaker direct beam which is surrounded by a system of concentric cones. These arguments might also be applied to the exit surface. Accordingly, from the superposition of all the cones, we expect a more or less uniform background in the CBED pattern.

As explained in §5.2, the fit program accounts for a uniform background. Since no new features are created in the CBED pattern, we do not expect the amorphous layer to be a serious problem. However, since electrons are scattered into the background, we count less electrons in the reflections. This will lead to a slight overestimation of the temperature factors. The corresponding error is hard to quantify. On the other hand, the thickness of the amorphous oxide layer is smaller than 2 nm (top and bottom surfaces), which is still very small compared with a total specimen thickness of about 40–100 nm.

### 7.4. *Lattice strain*

It is one of the major advantages of the electron microscope that it offers both imaging and diffraction modes. In the imaging mode, we may check the quality of the specimen area under investigation and look for an appropriate region. For NiAl, it is almost impossible to find large areas without lattice distortions caused, for example, by dislocations. Nevertheless, the focused beam used in the CBED technique allows a region that appears to be perfect to be selected. However, even far away from a dislocation, core strain might be present and thus a local variation of the lattice parameters.

In order to estimate the influence of the lattice strain on the temperature factors, we have to discuss the influence on the structure factors. These depend on the volume of the unit cell as well as on the length of the reciprocal-lattice vectors **g**. For high-angle scattering, the atomic form factor $f_i(\mathbf{g})$ is roughly proportional to $g^{-2}$. According to (1), the structure factors of a cubic system are then proportional to $1/a$. Therefore, a 1% change of the lattice constant $a$ will change each structure factor also by 1%.

To estimate this influence, we have to slightly modify (17). While the 'true' structure factor is given by

$$U_{\mathbf{g}} = (\alpha/\Omega)\{f_{\mathrm{Ni}} \exp[-\tfrac{1}{2}\langle u^2\rangle_{\mathrm{Ni}} g^2] \pm f_{\mathrm{Al}} \exp[-\tfrac{1}{2}\langle u^2\rangle_{\mathrm{Al}} g^2]\} \quad (18)$$

with $\alpha = 0.995$ (for a 0.5% increase of $a$, which indeed would be a rather large change), the program assumes $\alpha = 1.0$ and tries to compensate this by modifying the temperature factors. In this case, we would obtain an error $\Delta u/u$ smaller than 0.01, for both Ni and Al. Therefore, this error is negligible.

### 7.5. *Microscope aberrations*

As a result of the aberrations of the imaging energy filter as well as of the objective lens, we have two major effects on the CBED patterns. These are aberrations that distort the geometry of the pattern and those that affect the intensity.

The most important geometrical distortion is the anisotropic magnification of the CBED pattern, which, in our microscope, is of the order of 1%. As a consequence, the positions of the deficiency lines of higher-order Laue-zone reflections in the (000) disc are slightly modified and some accuracy in determining the exact beam orientation is lost. On the one hand, we can take care of this problem by simply fitting the anisotropic magnification. On the other hand, we found that for temperature-factor determination (but not for structure-factor determination) the accuracy is sufficient, even without taking the anisotropy into account. Therefore, geometrical distortions do not decrease the accuracy of the measurement.

In addition to the geometrical distortion, we have second-order chromatic aberrations of the energy filter. Accordingly, in each pixel of the CBED pattern we record a slightly different section of the energy spectrum as compared with the neighbouring pixel. As a consequence, only a limited angular range of a diffraction pattern can be recorded and used for quantitative evaluation at one time. This is the main reason why we do not use imaging plates for CBED at present.

The typical width of the energy selection window is 5 to 10 eV. Therefore, we might also record plasmon scattered electrons in some regions of the pattern. In a rough approximation, the scattering-angle distribution caused by plasmon losses is Lorentzian shaped, which means peaked in a forward-scattering direction. Therefore, if we had a significant plasmon signal in the pattern, it would be clearly visible in the minima next to the central rocking-curve maxima, where too much intensity would be detected. This effect was never observed. It is worthwhile mentioning that we always take two frames, one with the (000) disc and one with the **g** discs For both frames, the position of the energy-selecting slit is independently adjusted. Therefore, the influence of this error is minimized and a systematic deviation of the measured intensity from the simulation as described above was never found.

### 7.6. *Point spread function of the CCD camera*

The CBED patterns are recorded with a slow-scan CCD camera. This kind of two-dimensional detector usually shows a strong channel mixing (or cross talk) over a distance of about 10 pixels. We have tried to correct for this effect by deconvolution. However, since correcting for the channel mixing increases the noise level, we have slightly undercompensated and therefore some channel mixing is left in the pattern. As a consequence, even after the correction process the maxima in the dark-field discs are too low and there is too much intensity in the corresponding deficiency lines in the (000) disc. This results in an overestimation of the temperature factors.

In general, the error introduced hereby is hard to quantify. In order to get an estimate of the error, we determined for one case (which is the experimental example given in the previous section) the temperature factors with and without correcting for the channel mixing. We found that the temperature factors were changed by less than 1%. However, the background level of the bright-field disc was increased by almost a factor of 5, those of the dark-field discs by a factor of 1.5. This indicates that the fitted individual backgrounds can almost compensate for uncorrected cross-talk effects, even in the case of no correction at all. Since the remaining cross-talk effects after the corrections are almost negligible, the accuracy of the measurement is not affected by the channel mixing.

### 7.7. *Background estimation*

Although the CBED patterns are zero-loss energy filtered, there is unavoidably a background of electrons that have undergone thermal diffuse scattering. The corresponding intensity underlying the elastic signal in the discs is not uniform but structured. Unfortunately, this is not possible to simulate, if at all, in acceptable computing time. However, in our experiments on NiAl, it could be estimated from outside the discs that the ratio of elastic intensity:average background intensity:modulation of background intensity is of the order 1000:10:1. Therefore, as a simple and straightforward strategy, we assume constant background intensities $B_i$, which can vary for different discs $i$.

We cannot estimate the error of the temperature factors introduced by assuming a flat background rather than the real modulated one. However, in the case study we checked the influence of the available background-fitting techniques. First we fitted individual backgrounds as the best approximation to the experimental situation. Then we fitted one common level for all discs (*i.e.* $B_i = B$ for all $i$), resulting in a change of the temperature factors, $-0.12$ pm for Ni and $+0.35$ pm for Al. If the common level is set to zero (no background assumed), the TF of Ni changes by $-0.2$ pm, whereas the Al value is unchanged.

These results prove that there is a significant dependency of the results on the background. The change of the temperature factors as a function of the applied fitting technique is comparable with the scatter (standard deviation) of the results given in Table 1. It is clear that allowing the background level to vary from disc to disc is the best approximation currently available. However, the influence of the modulation is uncertain. Because it is likely to be an important error source, it demands further investigation.

The background signal depends on the beam orientation, specimen thickness and, *via* amorphous surface layers, also on the specimen itself. Therefore, we may regard the background influence partly as stochastic, although for given parameters the background is well defined.

## 8. Conclusions

A new technique has been described to measure temperature factors with high accuracy by means of convergent-beam electron diffraction. This technique is based on the automated matching of simulated data to a series of line scans extracted from several high-order dark-field discs and from the bright-field disc.

For the intermetallic phase NiAl, we found $u(\mathrm{Ni}) = 5.5 \pm 0.1$ and $u(\mathrm{Al}) = 5.7 \pm 0.1$ pm at 110 K. These values are obtained as the average over a set of seven experimental results. Since no other experimental data for this temperature have been reported so far, we can only compare our results with the theoretical calculations of Gumbsch & Finnis (1996). They found from a molecular dynamics simulation $u(\mathrm{Ni}) = 5.1$ and $u(\mathrm{Al}) = 5.2$ pm, which is in close agreement with our results.

In a detailed discussion, the error sources have been identified. The influence of each error source is discussed and quantified. The most important errors arise from the uncertainty in specimen stoichiometry as well as from the background underlying the elastic signal in the diffraction discs. Small deviations from the assumed composition, which are within the error bar of the wet chemical analysis, may lead to an error in the temperature factor. For the given experiment, this error is smaller than 0.1 pm. For each diffraction disc, an individual flat background has been considered as the dominant contribution. Less-accurate techniques led to a variation in the temperature factors of about 0.2 pm.

This work was financially supported by the Volkswagen-Stiftung (contract no. I/68313). We are indebted to R. Henes and U. Essmann for supplying the NiAl single crystals and to D. and P. Rez for sending us the atomic scattering amplitudes on floppy disk.

### References

Bird, D. M. & Saunders, M. (1992). *Acta Cryst.* A**48**, 555–562.
Burgess, W., Saunders, M., Bird, D. M., Preston, A. R., Zaluzec, N. J. & Humphreys, C. J. (1994). Proc. 13th International Congress on Electron Microscopy, Vol. I, pp. 847–848.
Cooper, M. J. (1963). *Philos. Mag.* **8**, 811–821.
Deininger, C., Necker, G. & Mayer, J. (1994). *Ultramicroscopy*, **54**, 15–30.
Doyle, P. A. & Turner, P. S. (1968). *Acta Cryst.* A**24**, 390–397.
Essmann, U., Henes, R., Holzwarth, U., Klopfer, F. & Büchler, E. (1997). *Phys. Status Solidi*. In the press.
Fox, A. G. (1983). *J. Phys. F: Met. Phys.* **13**, 1593–1605.
Georgopoulos, P. & Cohen, J. B. (1977). *Scr Metall.* **11**, 147–150.
Gumbsch, P. & Finnis, M. W. (1996). *Philos. Mag. Lett.* **73**, 137–144.
Hall, C. R. & Hirsch, P. B. (1965). *Proc. R. Soc. London Ser. A*, **286**, 158–177.
Holmestad, R., Weickenmeier, A. L., Zuo, J. M. & Horita, Z. (1993). Proc. 51st Annual Meeting of the Microscopy Society of America, pp. 698–699.
Holmestad, R., Weickenmeier, A. L., Zuo, J. M., Spence, J. C. H. & Horita, Z. (1993). *Inst. Phys. Ser.* No. 138, Section 3, pp. 141–144.
Holmestad, R., Zuo, J. M., Spence, J. C. H., Hoier, R. & Horita, Z. (1995). *Philos. Mag.* A**72**, 579–601.
Hughes, T. M., Lautenschlager, E. P., Cohen, J. B. & Brittain, J. (1971). *J. Appl. Phys.* **42**, 3705–3716.
Ingber, L. (1989). *Math. Comput. Modelling*, **12**, 967–973.
Lehmpfuhl, G., Krahl, D. & Uchida, Y. (1995). *Acta Cryst.* A**51**, 504–514.
Matsumara, S., Tomokiyo, Y. & Oki, K. (1989). *J. Electron Microsc. Tech.* **12**, 262–271.
Mayer, J., Eigenthaler, U., Plitzko, J. & Dettenwanger, F. (1997). *Micron.* Submitted.
Menon, E. S. K. & Fox, A. G. (1996). *Acta Mater.* **44**, 2547–2555.
Nüchter, W., Weickenmeier, A. L. & Mayer, J. (1995). *Inst. Phys. Ser.* No. 147, Section 4, pp. 129–132.
Preston, A. R., Burgess, W. G., Pickup, C. J. & Humphreys, C. J. (1993). *Inst. Phys. Ser.* No. 138, Section 3, pp. 145–148.
Reimer, L. (1984). *Transmission Electron Microscopy.* Berlin: Springer.
Rez, D., Rez, P. & Grant, P. I. (1994). *Acta Cryst.* A**50**, 481–497.
Sandakova, M. I., Sandakov, V. M., Kalishevich, G. I. & Gel'd, P. V. (1971). *Russ. J. Phys. Chem.* **45**(6), 901.
Spence, J. C. H. & Zuo, J. M. (1992). *Electron Microdiffraction.* New York: Plenum Press.
Swaminathan, S., Jones, I. P., Maher, D. M., Johnson, A. W. S. & Fraser, H. L. (1997). *Philos. Mag. Lett.* **75**, 261–270.
Weickenmeier, A. & Kohl, H. (1991). *Acta Cryst.* A**47**, 590–597.
Weickenmeier, A. L., Nüchter, W. & Mayer, J. (1995). *Optik (Stuttgart)*, **99**, 147–154.
Willis, B. T. M. & Pryor, A. W. (1975). *Thermal Vibrations in Crystallography.* Cambridge University Press.
Wolberg, J. R. (1967). *Prediction Analysis*. New York: van Nostrand.
Yoshioka, H. (1957). *J. Phys. Soc. Jpn*, **12**, 618–628.
Zuo, J. M., Holmestad, R., Tomokiyo, Y. & Yase, K. (1995). Proc. 53rd Annual Meeting of the Microscopical Society of America, pp. 138–139.
Zuo, J. M. & Spence, J. C. H. (1991). *Ultramicroscopy*, **35**, 185–196.
Zuo, J. M. & Weickenmeier, A. L. (1995). *Ultramicroscopy*, **57**, 375–383.